Bulletin of the Seismological Society of America, Vol. 70, No. 5, pp. 1893–1905, October 1980

PRE-, CO-, AND POSTSEISMIC STRAIN CHANGES ASSOCIATED WITH THE 1952 M_L = 7.2 KERN COUNTY, CALIFORNIA, EARTHQUAKE

BY W. SCOTT DUNBAR,* DAVID M. BOORE, AND WAYNE THATCHER

ABSTRACT

Triangulation surveys carried out in the vicinity of the White Wolf Fault in 1932, 1952, 1953, and 1963 are used to delineate the strain changes preceding, accompanying, and following the 1952 earthquake. The strain rate (engineering shear) during the preseismic interval (1932 to 1952) was 0.36 ± 0.10 μstrain/yr and was nearly uniform across the 70-km-long triangulation arc, with the plane of maximum left-lateral shear oriented N44° ± 7°E, nearly parallel to the White Wolf Fault. The coseismic observations (1952 to 1953), supplemented by leveling data, are matched using a dislocation model with the following characteristics

Dip = 60°SE

Strike = N50°E

Length = 70 km

Left-Lateral Strike-Slip = 2.4 ± 0.1 meter (m)

Reverse Dip-Slip = 1.9 to 0.6 m (decreasing to the NE)

Seismic moment ≧ 0.9 × 10^{27} dyne-cm.

The data also require most of the slip to have occurred below ~5 km (5 to 20 km in our model), on roughly the southwest half of the fault, with the slip occurring at shallow depths to the northeast. The postseismic triangulation data (1953 to 1963) indicate that the average shear strain rate in the 10 yr following the earthquake (0.80 ± 0.20 μstrain/yr) was about twice that during the 20 yr preceding it. The postseismic strain changes were concentrated closer to the fault than those determined for the preseismic time interval, and the 1953 to 1963 data are explained well by episodic postseismic slip of about 2 m (left-lateral strike-slip) occurring on the down-dip extension of the coseismic fault plane.

INTRODUCTION

The Kern County earthquake of July 21, 1952 is one of the most significant earthquakes to occur in the conterminous United States since 1906. Its magnitude (M_S = 7.4 to 7.7, Gutenberg, 1955b; M_L = 7.2, Kanamori and Jennings, 1978; Bolt, 1978) is larger than any event since the 1906 San Francisco earthquake. It occurred on the White Wolf Fault, to the north of the intersection of the Garlock and San Andreas faults (Figure 1). Although the White Wolf Fault was recognized as active, the occurrence of the earthquake came as a surprise and alerted people to the hazard associated with the range front faults in the vicinity of the "Big Bend" in the San Andreas Fault. The hazard was reemphasized by the occurrence of the 1971 San Fernando earthquake (M_L = 6.4).

Despite the importance of the earthquake and the availability of the data, surprisingly few geophysical studies have been made of this earthquake. Most of the

* Present address: Weidlinger Associates, 3000 Sand Hill Road, Building 4, Suite 245, Menlo Park, California 94025.

studies appeared in 1955 as *Bulletin 171* of the California Division of Mines (now the Division of Mines and Geology). In that volume, Gutenberg (1955a, b) used regional and teleseismic recordings to estimate the origin time, location, and magnitude. He found that *P*-wave first motions implied faulting on a plane dipping 63° in a direction S40°E. This roughly agreed with field and aftershock studies. The triangulation and leveling data were consistent with left-lateral, reverse faulting, but no attempt was made to fit the data to a model of the fault. The distribution of surface wave amplitudes showed an azimuthal variation which Benioff qualitatively explained by the directivity associated with northeasterly propagation of the fault rupture from the epicenter at the southern end of the fault.

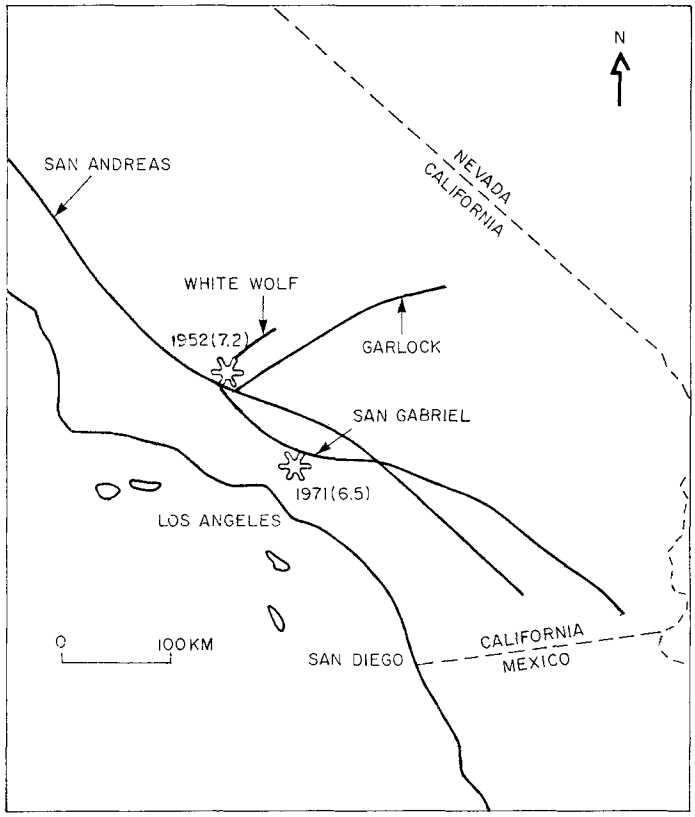

FIG. 1. Location of Kern County (1952) and San Fernando (1971) earthquakes. Major faults are named and denoted by an arrow.

In this paper we concentrate on interpretations of the triangulation data using recently developed methods for analyzing and modeling geodetic data.

ANALYSIS OF GEODETIC DATA

The data. Detailed geodetic surveys were made in the region before and after the Kern County earthquake. A triangulation network (Figure 2) was surveyed in 1932, in 1952 just before the event, in 1953, and again in 1963, thus providing information on the ground deformation in pre-, co-, and postseismic intervals. The coseismic interval spanned about 10 months. The basic data, given in Dunbar (1977), consist of direction lists for each survey, from which angle changes may be computed.

Leveling lines have been run repeatedly along two highways which run almost perpendicular to the fault trace and cross the trace at its north and south ends.

Although the observed angle changes are the basic data to be used in detailed inversion studies, it is often advantageous to use the shear strains averaged over various quadrilaterals in preliminary interpretations. We used a method described by Frank (1966) to estimate the engineering shear strains

$$\gamma_1 = e_{EE} - e_{NN}$$

$$\gamma_2 = e_{NE} + e_{EN}$$

where e_{NN} and e_{EE} are the north and east tensor normal strains, respectively, and

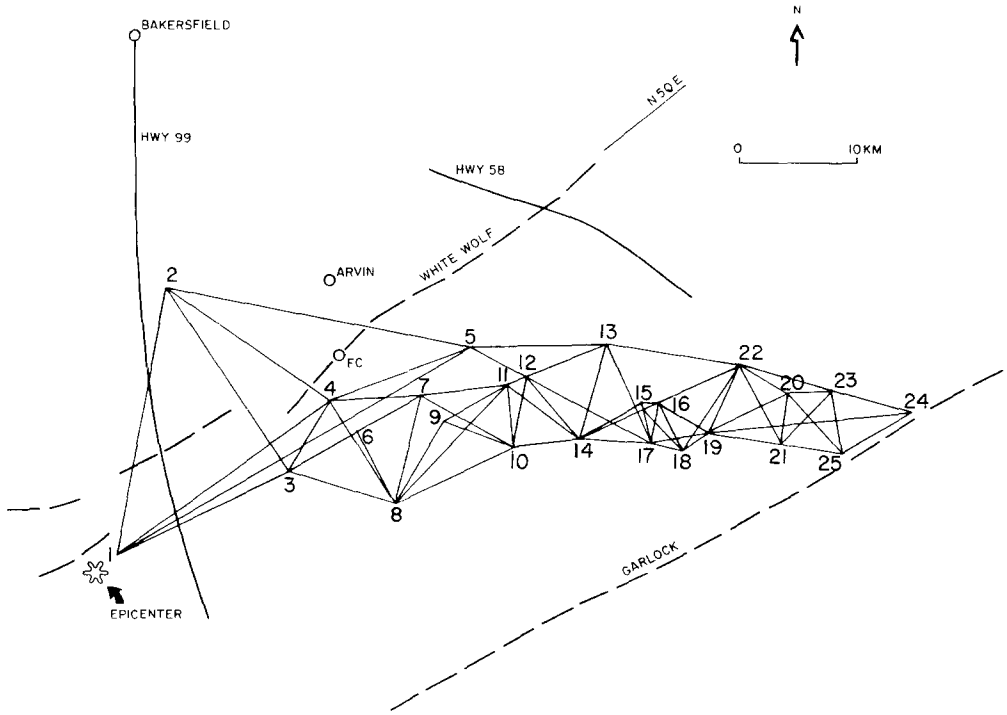

FIG. 2. Triangulation net and leveling survey routes along Highways 99 and 58. The numbered points are the triangulation stations. The point marked FC and the straight line marked N50E, respectively, denote the center and orientation of a 70-km-long dislocation model used to interpret the data.

e_{NE} and e_{EN} are the tensor shear strains. Given γ_1 and γ_2, estimates of the azimuth of elongation Ψ (clockwise from north, tensile strain being positive) and the total strain γ can be made using

$$\Psi = \frac{1}{2}\tan^{-1}\left[\frac{-\gamma_2}{\gamma_1}\right] \qquad \gamma = [\gamma_1^2 + \gamma_2^2]^{1/2}.$$

Estimates of γ_1 and γ_2 using both a standard least-squares estimator and one based on the absolute value norm (Claerbout and Muir, 1973) are given in Tables 1 to 3. This latter estimator is stable in the presence of gross errors in the data, and large differences in the values of γ_1 and γ_2 given by the two estimators may indicate the presence of spurious data.

TABLE 1

PRESEISMIC STRAIN ANALYSIS*

Polygon Stations	Distance from Fault (km)	Least Squares		Absolute Value Norm	
		γ_1	γ_2	γ_1	γ_2
2 4 5	−1.4	15 ± 1	0 ± 1	15	0
8 4 7	7.0	−1 ± 5	−2 ± 3	1	2
6 7 8	7.8	11 ± 4	−1 ± 4	10	−7
5 13 12	10.4	9 ± 2	18 ± 8	12	28
8 7 11 10	10.9	6 ± 5	4 ± 5	4	6
8 9 11 10	11.5	6 ± 6	1 ± 8	12	4
10 11 12 14	13.4	7 ± 7	3 ± 6	9	−2
14 12 13 17	15.9	8 ± 3	6 ± 3	5	6
14 13 17	17.4	2 ± 4	7 ± 2	5	4
15 16 18†	20.5	−1 ± 10	−14 ± 10	−1	−6
15 16 18 17	20.8	6 ± 8	−5 ± 7	1	−3
17 15 18†	21.3	−29 ± 26	−18 ± 10	3	−18
18 16 22 19	22.4	1 ± 3	3 ± 5	5	8
19 22 20	24.0	13 ± 1	−11 ± 1	12	−9
19 22 21†	25.0	−2 ± 3	−4 ± 3	−5	0
19 22 20 21	25.2	8 ± 5	−4 ± 6	10	0

* All strain estimates and standard errors are rounded to the nearest whole number. There is no standard error estimate for the absolute value norm.

† Not plotted in Figure 3.

TABLE 2

COSEISMIC STRAIN ANALYSIS*

Polygon Stations	Distance from Fault (km)	Least Squares		Absolute Value Norm	
		γ_1	γ_2	γ_1	γ_2
1 2 3	−2.7	31 ± 1	1 ± 1	31	1
3 2 4	−2.2	9 ± 5	17 ± 12	16	9
2 4 5	−1.4	49 ± 6	83 ± 18	42	87
2 4 3 1	−1.5	23 ± 7	1 ± 13	31	1
1 4 3	2.3	−50 ± 17	−41 ± 3	−67	−37
1 4 5	3.1	154 ± 76	−80 ± 54	56	−7
3 4 7 6*	4.4	120 ± 30	−38 ± 19	102	22
3 4 8	6.1	41 ± 1	−50 ± 2	40	−47
3 4 7 8	6.2	41 ± 12	−9 ± 13	44	3
8 4 7	7.0	56 ± 1	16 ± 1	58	16
3 6 8	7.0	22 ± 3	6 ± 4	23	12
6 7 8	7.8	0 ± 6	0 ± 6	−8	−5
5 13 12	10.4	−29 ± 1	7 ± 3	−28	11
8 7 11 10	10.9	−34 ± 8	−7 ± 8	−36	−5
8 9 11 10	11.5	−44 ± 5	−5 ± 6	−41	−12
10 11 12 14	13.4	−39 ± 5	6 ± 4	−32	7
14 12 13 17	15.9	−51 ± 2	1 ± 2	−52	1
14 13 17	17.4	−53 ± 2	−1 ± 1	−54	1
15 16 18†	20.5	5 ± 10	11 ± 9	17	24
15 16 18 17	20.8	7 ± 5	10 ± 4	5	3
17 15 18	21.3	32 ± 6	15 ± 2	40	15
18 16 22 19	22.4	−27 ± 2	−12 ± 4	−24	−7
19 22 20	24.0	−7 ± 6	5 ± 6	−12	13
19 22 21†	25.0	−2 ± 9	−5 ± 9	7	−16
19 22 20 21	25.2	−9 ± 4	−2 ± 5	−9	−2
21 20 23 25†	29.2	−5 ± 1	−4 ± 1	−6	−4
21 20 25	29.3	−3 ± 6	−5 ± 3	4	−10

* All strain estimates and standard errors are rounded to the nearest whole number. There is no standard error estimate for the absolute value norm.

† Not plotted in Figure 3.

The values γ_1 and γ_2 were arbitrarily assigned to the center of the appropriate quadrilateral. The data were then plotted as a function of perpendicular distance of the center of the quadrilateral from the fault. (This plotting is for convenience only and implies no assumption of two-dimensionality in the faulting, the interpretation being based on three-dimensional models.) Plotted error bars are one standard deviation values obtained in each case from a least-squares fit of the angle change data to a uniform strain field. Thus, the error bars represent both measurement errors and any actual departures from the assumed spatial uniformity of the strain field. The results are shown in Figure 3. Note the distinctive shape and amplitude

TABLE 3

POSTSEISMIC STRAIN ANALYSIS*

Polygon Stations	Distance from Fault (km)	Least Squares		Absolute Value Norm	
		γ_1	γ_2	γ_1	γ_2
1 2 3	−2.7	4 ± 4	1 ± 5	0	4
3 2 4	−2.2	−5 ± 3	25 ± 8	−10	31
2 4 5	−1.4	7 ± 1	−5 ± 1	7	−4
2 4 3 1	−1.5	2 ± 3	5 ± 6	1	4
1 4 3†	2.3	−26 ± 96	−8 ± 15	71	−30
1 4 5†	3.1	123 ± 219	−92 ± 155	406	−304
3 4 7 6	4.4	40 ± 27	−28 ± 17	35	−34
3 4 8†	6.1	12 ± 4	−10 ± 6	14	−18
3 4 7 8	6.2	17 ± 4	−3 ± 5	18	−4
8 4 7	7.0	23 ± 4	2 ± 3†	29	3
3 6 8	7.0	−1 ± 2	0 ± 3	−1	5
6 7 8	7.8	11 ± 1	10 ± 1	11	12
5 13 12	10.4	5 ± 1	−17 ± 1	5	−16
8 7 11 10	10.9	5 ± 4	2 ± 5	6	4
8 9 11 10	11.5	13 ± 2	3 ± 3	12	4
10 11 12 14	13.4	21 ± 4	−2 ± 3	26	−4
14 12 13 17	15.9	6 ± 4	6 ± 4	7	10
14 13 17	17.4	−3 ± 3	7 ± 2	−1	4
15 16 18	20.5	9 ± 4	6 ± 4	15	11
15 16 18 17	20.8	6 ± 4	5 ± 3	9	2
17 15 18	21.3	−20 ± 4	3 ± 1	−25	3
18 16 22 19	22.4	4 ± 3	2 ± 5	4	1
19 22 20	24.0	10 ± 4	−6 ± 4	13	−11
19 22 21†	25.0	−6 ± 1	−3 ± 1	−5	−4
19 22 20 21	25.2	0 ± 4	5 ± 4	−7	7
21 20 23 25†	29.2	10 ± 2	3 ± 2	9	4
21 20 25	29.3	4 ± 7	7 ± 4	−5	12

* All strain estimates and standard errors are rounded to the nearest whole number. There is no standard error estimate for the absolute value norm.

† Not plotted in Figure 3.

of the coseismic data as compared with that of the intervals before and after the main shock. Also note that the average engineering shear strain rate for the postseismic period (0.80 ± 0.2 μstrain/yr) is about twice that for the preseismic interval (0.35 ± 0.1 μstrain/yr). The preseismic rate is comparable to rate of strain accumulation along various parts of the San Andreas fault system (Thatcher, 1975a, b, 1979; Prescott *et al.*, 1979).

Leveling lines along State Highways 99 and 58 have been surveyed a number of times. Figure 4 shows the data for time period 1926 to 1952 (post-earthquake), assuming a fixed point at Bakersfield (data have been taken from a contour map in

Whitten, 1955). More detailed coseismic modeling using a more extensive set of leveling data has been recently carried out by Stein *et al.* (1981), and their results are consistent with the modeling carried out in this paper. That is, the 1952 coseismic

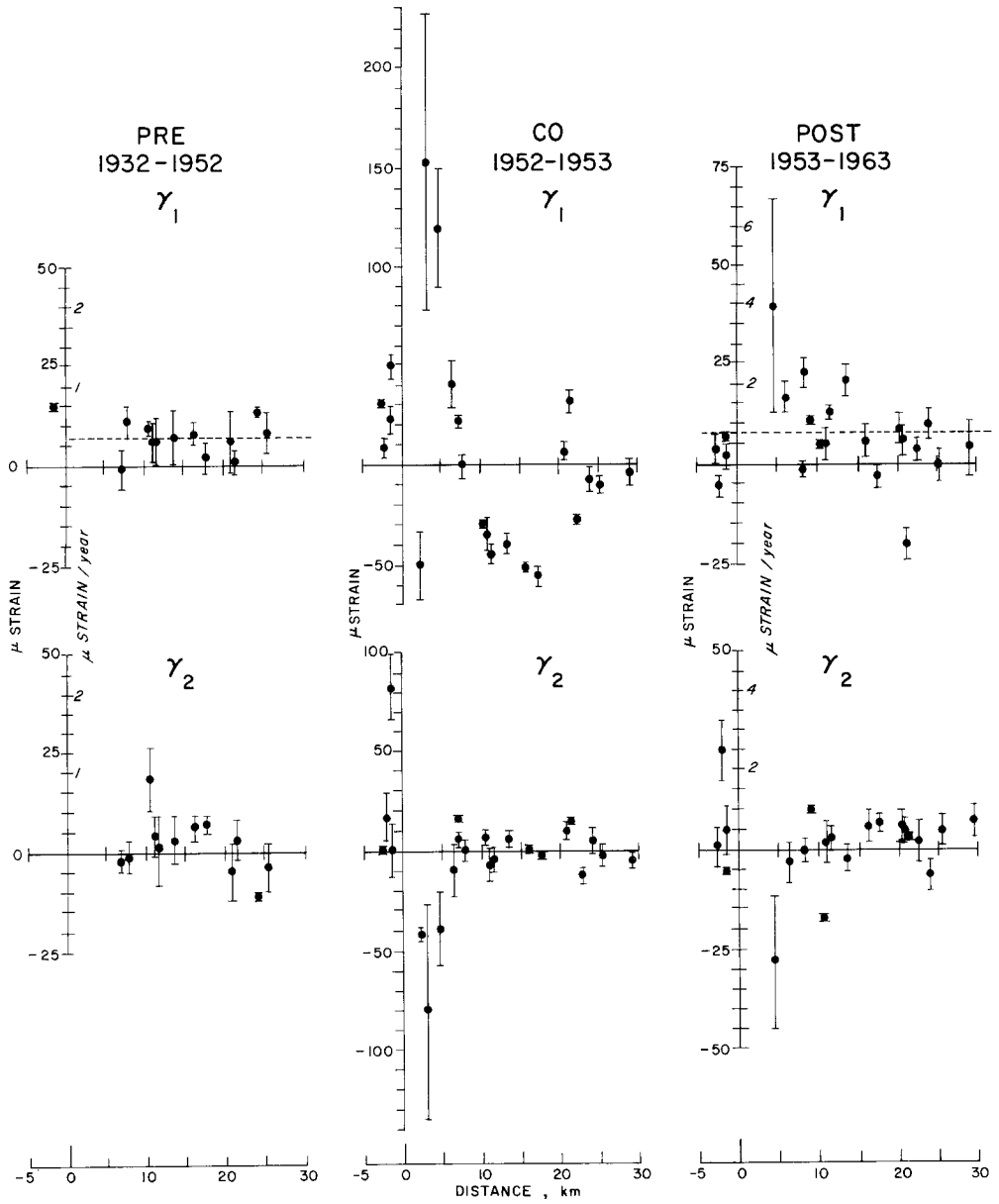

FIG. 3. Pre-, co-, and postseismic strain estimates for individual polygons of the triangulation net shown in Figure 2 (see Tables 1 to 3). The strains are plotted versus the perpendicular distance of the center of the polygon from the fault model shown in Figure 2. The bars denote the standard deviation of each estimate. Ordinate units are μstrain; units of μstrain/yr are also shown for pre- and postseismic intervals.

slip decreases in magnitude and occurs at successively shallower depths toward the northeast along the White Wolf Fault.

Preliminary interpretation. The series of theoretical curves in Figure 5 are useful

for a preliminary interpretation. These curves are derived from formulas given in Mansinha and Smylie (1971). Shown are γ_1 and γ_2 as a function of distance along a line perpendicular to the mid-point of a 70-km fault dipping 60° in the direction S40°E. The fault orientation and length were taken from studies of Gutenberg

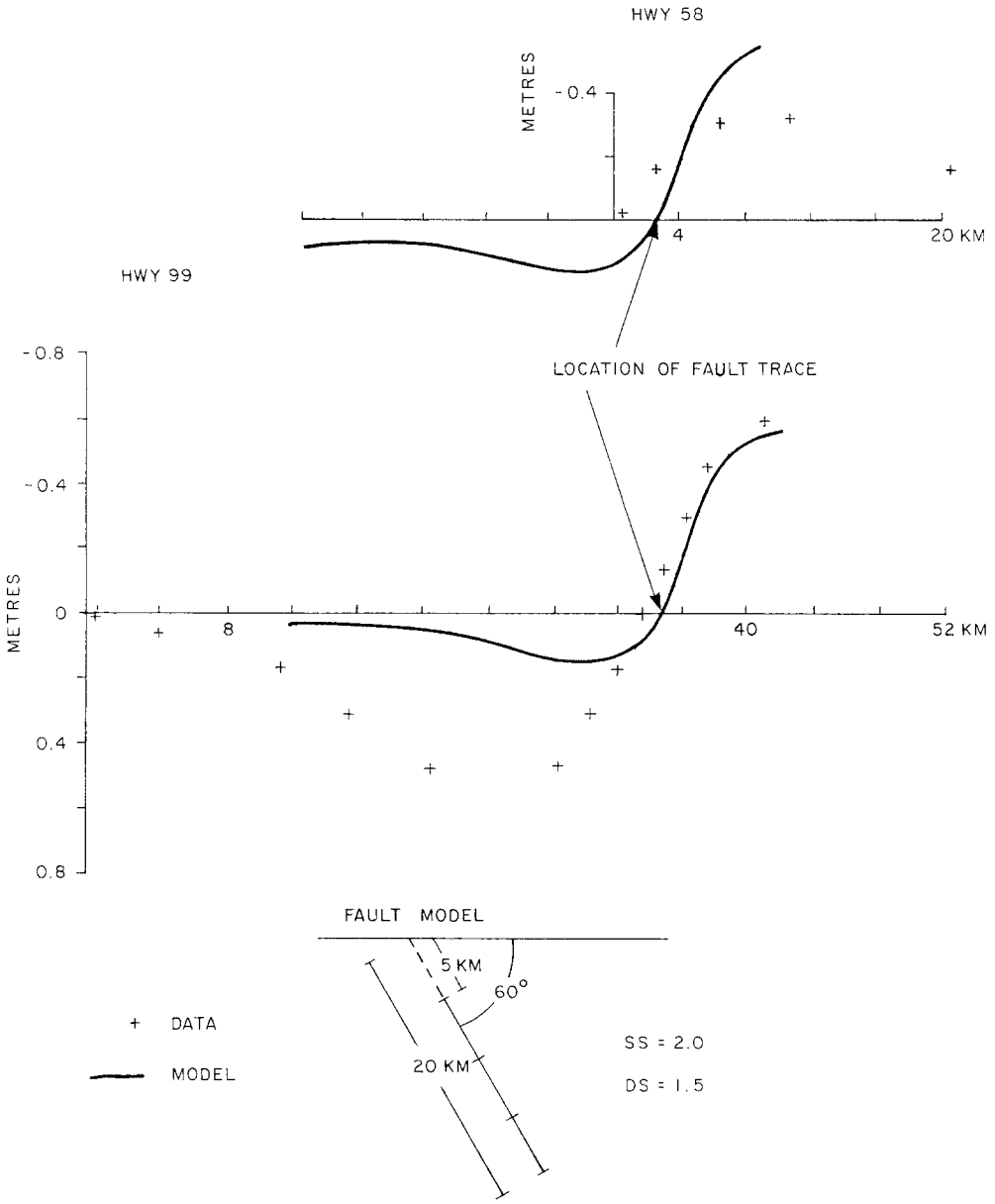

FIG. 4. Profiles of leveling data along Highways 99 and 58 (see Figure 2). Also shown is a cross-sectional view of the fault model used in modeling the data along Highway 99.

(1955a) and Richter (1955). The curves shown are the contributions for constant slip on different segments of the fault surface. First, for the orientation of the White Wolf Fault, except for end effects γ_1 should be near zero for pure reverse dip-slip faulting. Similarly, γ_2 will be near zero for pure left-lateral strike-slip faulting. This approximate "decoupling" between the two shear strain components thus allows us

to use the horizontal deformation measured at the free surface to estimate both components of fault slip. Second, the depth at which the faulting occurs has a pronounced influence on the shape of the curves; note that γ_1 is strongly negative near the fault only if the slip extends to the earth's surface. Both the pre- and

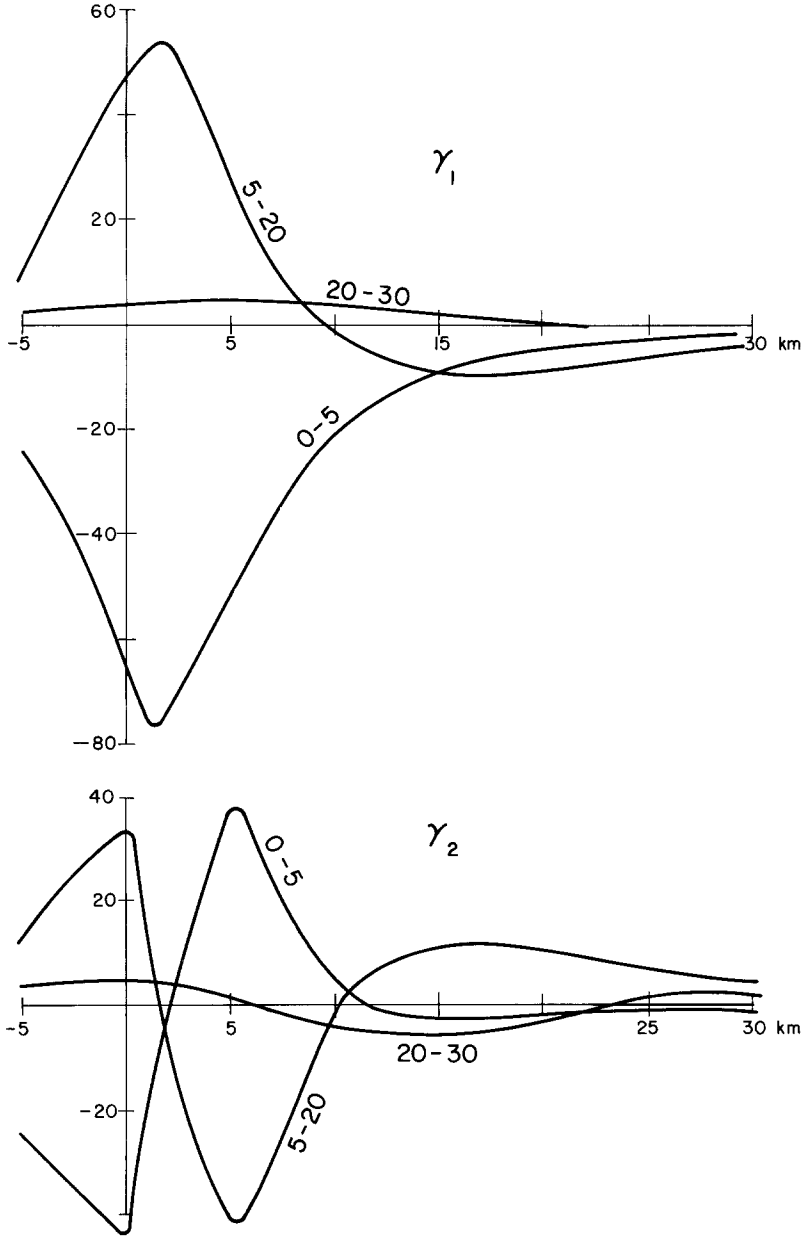

FIG. 5. Strain profiles along the perpendicular bisector of a 70-km-long dislocation with strike N50°E and dip 60°. One meter of left-lateral strike-slip and reverse dip-slip is imposed. The numbers next to each curve denote the down-dip extent of the dislocation segment. Strain is measured in μstrain.

postseismic slip can be explained by 1 to 2 m of left-lateral fault slip below a depth of about 15 km, with a slight indication from the distance decay of the postseismic γ_1 data that the postseismic slip was at shallower depths than the preseismic slip (assuming that the preseismic strain was due to slip on a fault; the data could

equally well be fit by uniform strain accumulation). The lower depth of the slip zone is poorly resolved by the data.

The coseismic data clearly require both left-lateral strike-slip and reverse slip on the fault surface. The slip was at shallower depths than inferred for the pre- and postseismic intervals, but the large positive values of γ_1 near the fault trace require that the slip near the Earth's surface be less than that at depth. A rough fit to the data is given by about 1.5 m of reverse slip and 2 m of left-lateral strike-slip between 5 and 20 km depth. The fit of this model to the leveling data is shown in Figure 4. The mismatch in the area of down dropping is not significant; this area corresponds to the southern end of the San Joaquin Valley, in which subsidence occurred due to withdrawal of oil and water. If the choice of the zero reference is valid, Figure 4 suggests that a lateral variation in the dip-slip movement occurred with less

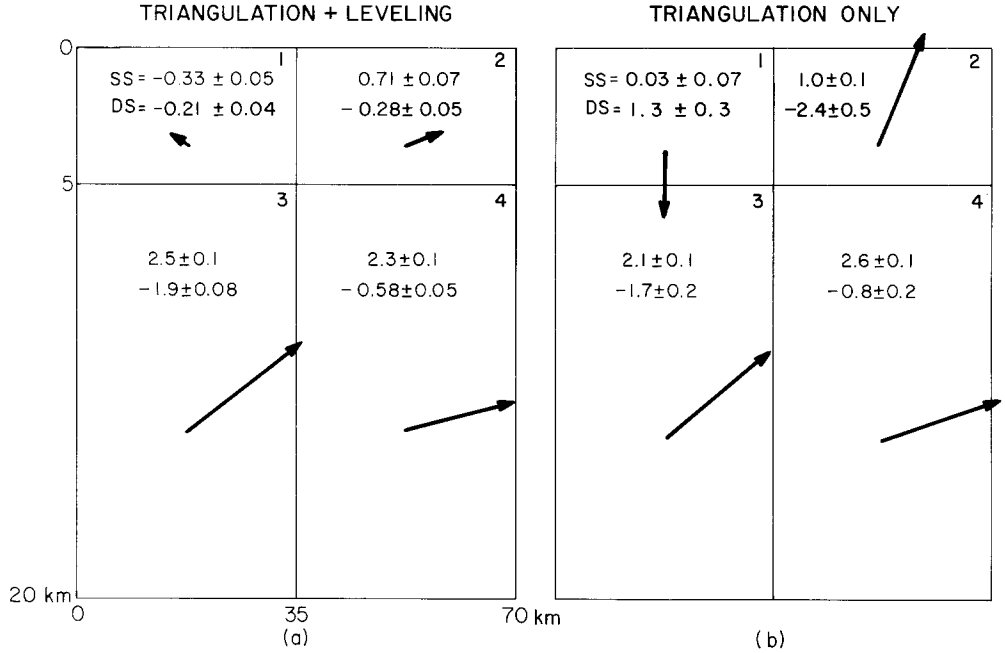

FIG. 6. (a) Slip estimates using both triangulation and leveling data. The *upper* number in each segment is the strike-slip (SS) in meters ($SS > 0$, left lateral). The *lower* number is the dip-slip (DS) in meters ($DS < 0$, thrust). The arrows show the direction and relative magnitude of the motion. (b) Slip estimates for triangulation data only.

movement at the northeast end of the fault than in the vicinity of the hypocenter, a conclusion supported by the recent detailed analysis of Stein *et al.* (1981).

Detailed modeling. A more detailed interpretation of the coseismic data was made using a least-squares procedure to fit various finite dislocation models of the coseismic faulting to the observed angle changes, the leveling data from the five southernmost stations on the HW 99 line, and all of the data for the HW 58 line (station locations are shown in Figure 2). A total of 103 angle changes and 10 elevation changes were used in the inversion. The standard error of the angle changes was taken to be 0.72 sec of arc and that of the leveling data was assumed to be 0.03 m. The model angle changes were based on the theoretical displacements of the triangulation stations.

To allow for the spatial variation of fault slip suggested in the interpretation above, the fault surface was divided into four segments. The segmentation and the derived slip is shown in Figure 6a when both angle changes and leveling data are

included. Figure 6b shows the results using the triangulation data only. As expected from the earlier interpretation, the slip is greater at depth, and the dip-slip component is smaller for the northeastern fault segment. In Figure 6a and b the strike-slip component is larger than the dip-slip component, although it has about equal parts near the hypocenter. As Boore and Kanamori (unpublished data) show, this is

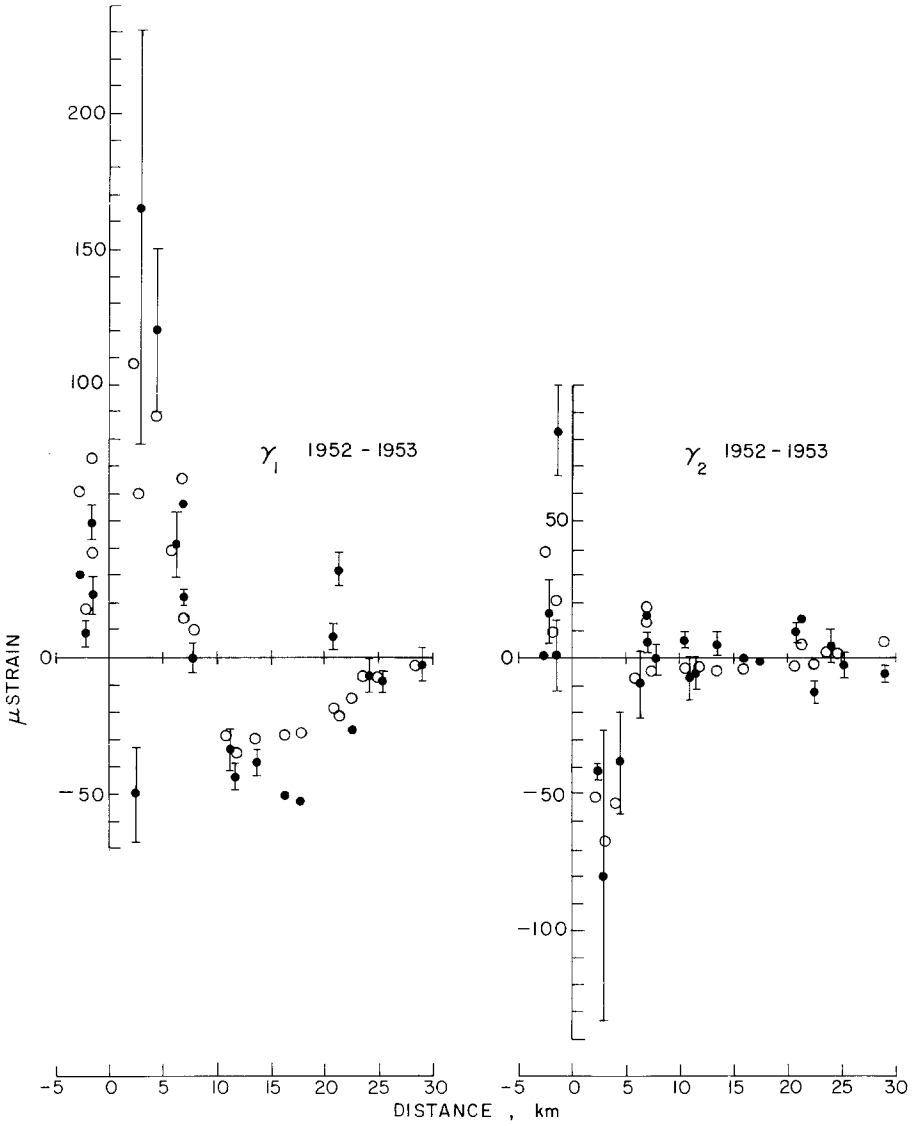

FIG. 7. Strain estimates (open circles) corresponding to the four-segment dislocation model shown in Figure 6, compared to the coseismic strain estimates (solid dots, with error bars), for individual polygons of the triangulation net shown in Figure 2. The data and theory for a given polygon are plotted at the same distance unless one would obscure the other.

consistent with other seismic data. Also note that the slip on the fault segment intersecting the earth's surface is larger in the northeastern half of the fault. This agrees with the geological observation that the surface fracture was more clearly developed at the northeast end of the fault.

Frank's method was used to compute the values of γ_1 and γ_2 predicted by the model. The computed strains are compared with the data in Figure 7. Generally, the

fit to the data is good. The large positive γ_1 strains at about 20-km distance can only be produced by localized slip. No particularly large aftershocks were located in this area, however, and the origin of these anomalous strains is problematic.

Formal tests of the following hypotheses were performed using methods described in the Appendix: (1) the strike-slip motion was zero on segment 1; (2) the dip-slip motion was equal in segments 3 and 4; and (3) the strike-slip motion was equal in segments 3 and 4. The first hypothesis was marginally acceptable, the second was strongly rejected, and the third was accepted. This gives added support to the decrease of the dip-slip motion in the northeastern part of the fault.

The seismic moment for the slip model in Figure 6a is 1×10^{27} dyne-cm (using a rigidity of 3.4×10^{11} dyne/cm^2). From the moment-magnitude relation of Thatcher and Hanks (1973) and aftershock information given by Richter (1955), we have estimated that 20 cm of the slip was due to aftershocks, leaving a moment of 0.9×10^{27} dyne-cm. The slip on the lower part of the fault is poorly resolved, and for this reason the derived moment should be considered a lower bound. Estimates of moment have been made from other types of data: Boore and Kanamori (unpublished data) found $M_0 \sim 1$ to 2×10^{27} dyne-cm using records from a low magnification instrument in Pasadena and teleseismic shear waves, Ben-Menahem (1978) determined a potency equivalent to a moment of 0.9×10^{27} dyne-cm from a simplified analysis of 20-sec surface waves, and Hanks *et al.* (1975) used the isoseismal map to estimate a moment of 2×10^{27} dyne-cm. Considering the various types of analyses, the poor resolution of the slip at the bottom of the fault from the geodetic data, and the likelihood that the slip was not uniform on the fault, the various estimates of moment are remarkably similar.

Acknowledgments

We thank W. B. Joyner for pointing out some typographical and drafting errors in the original manuscript.

This research was supported by the Division of Earth Sciences, National Science Foundation, Grant EAR76-02597.

Appendix: Hypothesis Tests

To obtain a more quantitative idea of how well the model fits the data and the amount of variation of slip required in the model, statistical methods were used to test hypotheses about the estimated slip. Using least-squares techniques, the mathematical problem is to solve the problem

$$\boldsymbol{d} = A\boldsymbol{x} + \boldsymbol{e}$$

subject to

$$B\boldsymbol{x} = \boldsymbol{c}$$

where $\boldsymbol{d}$ is an $\boldsymbol{m}$ vector of the data, A is a $m \times n$ model matrix, $\boldsymbol{x}$ is an $\boldsymbol{n}$ vector of the unknown slip on each fault segment, and $\boldsymbol{e}$ is a vector containing the errors associated with each datum in $\boldsymbol{d}$. B is a $k \times n$ matrix ($k < n$) and $\boldsymbol{c}$ is a $\boldsymbol{k}$ vector which describes the hypothesis to be tested in terms of equality constraints on the solution x. The hypothesis

$$H_0: Bx = c$$

is tested by computing the statistic

$$F = \frac{(\mathrm{SSC} - \mathrm{SSE})/k}{\mathrm{SSE}/(m - r)}$$

which has an F distribution with k and $m - r$ degrees of freedom. SSC is the error sum of squares of the constrained model, SSE that of the unconstrained model, k is the rank of B, m is the number of rows of A which is of rank r. When this statistic is computed, it is compared with tabulated values of F. The hypothesis H_0 is rejected if and only if

$$F \geqq \text{tabulated } F_{k,m-r} \text{ at the 5 per cent level.}$$

Details of this method may be found in Searle (1971). Lawson and Hanson (1974) describe algorithms for solving the least-squares problem with equality constraints.

The following hypotheses were tested

1. $SS_1 = 0$; zero strike-slip in segment 1
2. $DS_3 = DS_4$; equal dip-slip in segments 3 and 4
3. $SS_3 = SS_4$; equal strike-slip in segments 3 and 4.

TABLE 4

KERN COUNTY HYPOTHESES*

Hypothesis	SSC	SSE	$F = \frac{(\mathrm{SSC} - \mathrm{SSE})/k}{\mathrm{SSE}/(m - r)}$	$F_{k,m-r,0.05}$	Result
$SS_1 = 0$ ($k = 1$)	1007	954	5.8	3.9 ($F_{1,105,0.01} = 6.9$)	Marginal
$DS_3 = DS_4$ ($k = 1$)	1162	954	22.9	3.9	Reject
$SS_3 = SS_4$ ($k = 1$)	957	954	0.33	3.9	Accept

* $m - r = 113 - 8 = 105$. All sums of squares are dimensionless.

if the model matrix A is arranged such that the slip estimates in the vector $\boldsymbol{x}$ are in the following form

$$\boldsymbol{x}^t = [\mathrm{SS}_1, \mathrm{DS}_1, \mathrm{SS}_2, \mathrm{DS}_2 \ldots, \mathrm{SS}_4, \mathrm{DS}_4],$$

then hypothesis 1 is tested by making B a 1×8 matrix with the (1, 1) element equal to 1 and $\boldsymbol{c} = 0$. The second hypothesis is tested by making B a 1×8 matrix with the (1, 6) element equal to 1 and the (1, 8) element equal to -1. The vector $\boldsymbol{c}$ is again equal to zero. The equality constraints for the third hypothesis are constructed in a similar fashion.

The results of the tests are shown in Table 4. Hypothesis 1 was found to be marginally acceptable; i.e., if a 1 per cent significance level was chosen, it would be acceptable. Hypothesis 2 was found unacceptable, while the third hypothesis was accepted.

REFERENCES

Ben-Menahem, (1978). Source mechanism of the 1906 San Francisco earthquake, *Phys. Earth Planet. Interiors* **17**, 163–181.

Bolt, B. A. (1978). The local magnitude M_L of the Kern County earthquake of July 21, 1952, *Bull. Seism. Soc. Am.* **68,** 513–515.

Claerbout, J. F. and F. Muir (1973). Robust modeling with erratic data, *Geophysics* **38,** 826–844.

Dunbar, W. S. (1977). The determination of fault models from geodetic data, *Ph.D. Thesis*, Stanford University, Stanford, California, 201–213.

Frank, F. C. (1966). Deduction of earth strains from survey data, *Bull. Seism. Soc. Am.* **56,** 35–42.

Gutenberg, B. (1955a). The first motion in longitudinal and transverse waves of the main shock and the direction of slip. *Bull. 171, Calif. Div. Mines and Geol.*, 165–170.

Gutenberg, B. (1955b). Magnitude determination for larger Kern County shocks, 1952; effects of station azimuth and calculation methods, *Bull. 171, Calif. Div. Mines and Geol.*, 171–175.

Hanks, T. C., W. Thatcher, and J. A. Hileman (1975). Seismic moments of the larger earthquakes of the southern California region, *Bull. Geol. Soc. Am.* **86,** 1131–1139.

Kanamori, H. and P. C. Jennings, (1978). Determination of local magnitude, M_L, from strong-motion accelerograms, *Bull. Seism. Soc. Am.* **68,** 471–485.

Lawson, C. L. and R. J. Hanson (1974). *Solving Least Squares Problems*, Prentice-Hall, Inc., New Jersey, 134–143.

Mansinha, L. and D. E. Smylie (1971). The displacement fields of inclined faults, *Bull. Seism. Soc. Am.* **61,** 1433–1440.

Prescott, W. H., J. C. Savage, and W. T. Kinoshita (1979). Strain accumulation rates in the western United States between 1970 and 1978, *J. Geophys. Res.* **84,** 5423–5436.

Richter, C. F. (1955). Foreshocks and aftershocks, *Bull. 171, Calif. Div. Mines and Geol.*, 177–197.

Searle, S. R. (1971). *Linear Models*, John Wiley and Sons, Inc, New York, 110–113.

Stein, R. S., W. Thatcher, and R. O. Castle (1981). Late Quaternary and modern deformation along the fault-bounded northwest margin of the southern California uplift. *J. Geophys. Res.* **86,** (in press).

Thatcher, W. (1975a). Strain accumulation and release mechanism of the 1906 San Francisco earthquake, *J. Geophys. Res.* **80,** 4862–4872.

Thatcher, W. (1975b). Strain accumulation on the northern San Andreas fault zone since 1906, *J. Geophys. Res.* **80,** 4873–4880.

Thatcher, W. (1979). Horizontal crustal deformation from historic geodetic measurements in southern California, *J. Geophys. Res.* **84,** 2351–2370.

Thatcher, W. and T. C. Hanks (1973). Source parameters of southern California earthquakes, *J. Geophys. Res.* **78,** 8547–8576.

Whitten, C. A. (1955). Measurements of earth movements in California, *Bull. 171, Calif. Div. Mines and Geol.*, 75–80.

DEPARTMENT OF GEOPHYSICS
STANFORD UNIVERSITY
STANFORD, CALIFORNIA 94305 (W.S.D., D.M.B.)

U.S. GEOLOGICAL SURVEY
345 MIDDLEFIELD ROAD
MENLO PARK, CALIFORNIA 94025 (D.M.B., W.T.)

Manuscript received March 13, 1980